Silicon-Micromachined Flow Sensors

Thesis by

Fukang Jiang

In Partial Fulfillment of the Requirements

for the Degree of

Doctor of Philosophy

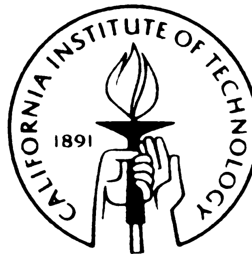

California Institute of Technology

Pasadena, California

1998

(Submitted July 17, 1997)

© 1998
Fukang Jiang
All rights reserved

To my beloved parents and wife

Acknowledgments

I would like to thank all the people that have supported and helped me during the six years of study and research at Caltech. In particular, I would like to acknowledge my academic advisor, Dr. Yu-Chong Tai. It was Dr. Tai who brought me into this exciting field of micromachining. More importantly, he has provided the key ideas, professional guidance and supports through all these years that made this work successful. I have also received tremendous help and valuable advice from Dr. Chih-Ming Ho, professor at the Department of Mechanical and Aerospace Engineering, University of California at Los Angeles, and the prime investigator of all the research projects involved in this work.

I thank the fellow members of the research project teams at UCLA, especially Dr. Steve Tung and Vincent Lee who gave me numerous help on the sensor characterization and on the understanding of the basic concepts in fluid dynamics. This thesis would not be complete without their efforts. I am also indebted to Wen Li, Karan Rainer and Michael Garstenauer who helped me in using the wind-tunnel at UCLA for the testing of the hot-wire anemometers.

I also thank my research partners in our group, Tom Tsao who has been working closely with me on two projects in the recent two years and proofread most chapters of the thesis, and Ken Walsh, who impressed me with his great photo-taking skill for small samples and helped me in the development of the flexible skins.

I deeply appreciate the past fellow members of our Lab, Drs. Jianqiang Liu, Chang Liu and Raanan Miller, for their many useful help in using the computers, design tools and processing equipment. The same thanks also go to all of the current fellow members of our group, especially Charles Grosjean, Shuyun Wu, Wen Hsieh, John Wright and Xuanqi Wang, and the guests of the group, Drs. Weilong Tang and Hsu-Tseng Yang. I am also grateful to our technician, Mr. Trevor Roper, who maintains all the processing equipment in good condition with his diligence and skill.

My thanks also go to our collaborators in Dr. Rodney Goodman's Microsystem Group at Caltech, Dr. Bhusan Gupta and Vincent Koosh, for the circuit and layout design of the M^3 system.

I would like to thank the Defense Advanced Research Programs Agency (DARPA) and the Air Force Office of Scientific Research (AFOSR) for providing me the financial support in the past four years.

Finally, I would like to thank my wife, Heng Ji, for her support and patience in the preparation of the thesis, and my parents for their constant encouragement over the many years of my education.

Silicon-Micromachined Flow Sensors

By

Fukang Jiang

In Partial Fulfillment of the Requirements

for the Degree of

Doctor of Philosophy

Abstract

A new generation of silicon-micromachined or micro-electro-mechanical-system (MEMS) sensors for the general purpose of microflow measurement and control is presented here. The first one is a polysilicon hot-wire anemometer made by a combined bulk and surface micromachining process. The new devices feature batch-fabricated free-standing micro polysilicon hot wires that are similar to conventional metal hot wires. Both the theoretical analysis and experimental (steady-state and dynamic) results show that MEMS hot wires have order-of-magnitude better frequency response, finer spatial resolution, and higher sensitivity over conventional hot-wire anemometers.

A novel MEMS thermal shear-stress sensor featuring vacuum-cavity insulation has been developed. The device is a polysilicon wire thermistor embedded in a silicon-nitride diaphragm which sits on top of a vacuum cavity. The vacuum cavity is to improve the thermal isolation between the polysilicon wire and substrate. To characterize the devices, both steady-state and transient heat-transfer theories have been established and used to calibrate wind-tunnel results, temperature sensitivities and frequency responses. Shear-stress sensor array chips have also been developed. Each of the shear-stress imagers has more than 100 sensors integrated on a 1×2.85 cm^2 chip. Our measurement results from a fully developed 2-D channel flow are well agreeable with previously published results.

For the first time, real-time 2-D wall shear-stress images in a turbulent flow have been experimentally obtained.

A new technology for the integration of micro-sensors, micro-actuators and microelectronics (M^3) on a single chip has been explored. Prototype M^3 chips including shear-stress sensors, magnetic actuators and CMOS circuits have been fabricated. This technology sets a base for the future development of a fully functional M^3 chip drag reduction.

Finally, a novel flexible MEMS skin technology fully compatible with IC process has been developed. Mechanically, the skin is made of metal leads sandwiched between polyimide layers that connect a number of silicon islands together. The skin can be applied conformablly on non-planar surfaces. The first application of this technology is a flexible shear-stress sensor skin that has been successfully used for the real-time measurement of shear-stress distribution on the leading edge of a delta wing model.

Table of Contents

1 Introduction

1.1 Fluid Mechanics Measurements 1

1.2 Flow Control 2

1.2.1 Basic Fluid Mechanics Concept 2

1.2.2 Flow Control 5

1.3 MEMS and Its Application in Fluid Mechanics 6

1.3.1 Silicon Micromachining 7

1.3.2 Integration with IC 8

1.3.3 MEMS in Fluid Mechanics 9

1.4 Overview of Chapters 9

Bibliography 11

2 Micromachined Hot-Wire Anemometers

2.1 Introduction 14

2.2 Design and Fabrication 16

2.2.1 Structures and Materials 16

2.2.2 Fabrication Process 18

2.2.3 Corner Compensation 20

2.2.4 Packaging 22

2.3 Steady-State Characteristics 22

2.3.1 Operation Modes and Operating Points 22

2.3.2 Sensitivity to Velocity 23

2.3.3 King's Law 26

2.4 Dynamic Characteristics 30

2.4.1 Time Constant Measurement 30

2.4.2 Transient Analysis 32

2.4.3 Constant Temperature Operation 34

2.5 Directional Dependency 38
2.6 Discussion 43
2.6.1 Comparison with Conventional Hot Wires 43
2.6.2 Small Aspect-Ratio Wires 44
2.6.3 Center-Lightly Doped Hot Wires 44
2.6.4 Mechanical Rigidity 45
2.6.5 Bending of Support Shanks 45
2.6.6 Temporal Drift 46
2.7 Summary 47
Bibliography 48

3 Micromachined Shear Stress Sensors
3.1 Introduction 50
3.2 Design And Fabrication 51
3.3 Heat Transfer Analysis 55
3.4 Calibration and Analysis 62
3.4.1 *I-V* Measurement 62
3.4.2 Temperature Sensitivity 66
3.4.3 Sensitivity to Shear Stress 69
3.4.4 Frequency Responses in CC Mode 75
3.4.5 Frequency Responses in CT Mode 81
3.5 Comparison with Conventional Hot-Film Sensors 89
3.6 Other Structures 89
3.6.1 Frequency Responses 91
3.6.2 Thermal Resistance 92
3.6.3 Steady-State Responses 94
3.7 Summary 95
Bibliography 96

4 Shear Stress Imager

4.1 Turbulent Boundary Layer and Streamwise Vortices 99

4.1.1 Channel Flow 99

4.1.2 Wind Tunnel 100

4.1.3 Streamwise Vortices and Sub-Layer Structures 101

4.2 Shear Stress Imager 103

4.3 Packaging, Biasing and Calibration 104

4.4 Shear Stress Imaging 108

4.5 Underwater Measurement 116

4.6 Summary 119

Bibliography 120

5 M^3 System for Viscous Drag Reduction

5.1 Skin-Friction Drag Reduction 122

5.2 MEMS Skin-Friction Drag Reduction Approach 123

5.3 System Integration 125

5.4 Conclusion 130

Bibliography 131

6 Flexible MEMS Technology and Shear Stress Sensor Skin

6.1 Introduction 133

6.2 Flexible Skin Technology 134

6.3 Flexible Shear Stress Sensor Array 139

6.4 Packaging and Calibration of the Shear Stress Sensor Skin 143

6.5 Measurement on Delta Wing 147

6.6 Sensor-Actuators Skin and Conformable M^3 System 152

6.7 Summary 154

Bibliography 156

A Description of Fabrication Processes

A.1 Micromachined Hot-Wire Anemometer 158
A.2 Micromachined Shear Stress Sensor 160
A.3 M^3 System 162
A.4 Flexible Shear Stress Sensor Array 165

List of Figures

1.1 Flow over (a) blunt-nosed body, (b) round-nosed body and (c) airfoil. 5
2.1 Schematic of a conventional hot-wire probe. 15
2.2 Schematic of the micromachined hot-wire probe.. 17
2.3 The temperature coefficient of boron doped ($2\times10^{20}cm^{-3}$) polysilicon resistors (50 squares) under different deposition and annealing conditions.......... 17
2.4 Simplified process flow with cross-sections for the fabrication of the micromachined hot-wire anemometers. 19
2.5 SEM pictures of (a) a 70 µm long hot wire and (b) a multiple-wire probe. 20
2.6 Photograph of tilted hot wires. 20
2.7 Long corner compensation structures on the front side for a 10 hour or more EDP etching. 21
2.8 Prototype of packaged hot wires. 22
2.9 Output characteristics of a 80 µm long hot wire in CC mode. 24
2.10 Output characteristics of the 80 µm long hot wire in CT mode. 25
2.11 Response of a conventional hot wire (5 µm in diameter, 1mm in length) in CC mode. The currents are 10 mA, 13 mA and 14 mA respectively for over-heat ratios of 0.15, 0.25 and 0.35. 25
2.12 Output voltages at the air flow velocity of 27 m/s for hot wires with different lengths in CT mode. 26
2.13 Simplified constant temperature bias circuit. 29
2.14 The constant current anemometer circuit for time constant measurement and wind-tunnel testing. 31
2.15 Square wave response of a 200 µm long hot wire in CC mode. 31
2.16 AC resistance change of a 10 µm long hot wire in the frequency domain. 32
2.17 Time constant in CC mode of the micromachined hot wires with different wire lengths. 34

2.18 Frequency response of a 10 μm long hot wire in CT mode. 37

2.19 Square wave response of the 10 μm long hot wire in CT mode. 37

2.20 Frequency bandwidths of the micromachined hot wires with different lengths in CT mode. 38

2.21 (a) Definition of yaw angle θ, pitch angles ϕ and roll angle ψ. (b) Cross section of micromachined hot wires.. 39

2.22 Yaw angular dependency of a 160 μm long hot wire in CT mode........................ 40

2.23 Yaw angular dependency of a 20 μm long hot wire in CT mode.......................... 40

2.24 Pitch angular dependency of the 160 μm long hot wire (also used in Figure 2.22) in CT mode. 41

2.25 Pitch angular dependency of a 20 μm long hot wire (also used in Figure 2.23) in CT mode. 42

2.26 Steady-state characteristics of an 80 μm long hot wire (also used in Figs. 2.9 and 2.10) in CT mode at different pitch angles... 42

2.27 SEM pictures of hot wires made from (a) polysilicon deposited at 620°C; (b) crystallized amorphous silicon deposited at 560°C. 45

2.28 The temporal drift of a 80 μm long hot wire at V = 2.5 V and a_R = 0.35............. 46

3.1 Cross-section of the micromachined shear stress sensor...................................... 52

3.2 Fabrication process flow of the micromachined shear stress sensor.................... 54

3.3 SEM picture of a micromachined shear stress sensor. The polysilicon resistor is 150 μm long and 3 μm wide. The nitride diaphragm is 200×200 μm^2. The sensor size is less than 300×300×550 (thickness) μm^3. Note that the entire sensor was in vacuum of the SEM sample chamber so the diaphragm in the picture is flat.. 54

3.4 Geometry of the diaphragm and the sensing wire. 55

3.5 (a) Symbol of the shear stress sensor. (b) Equivalent ac circuit model................ 62

3.6 The measured resistance-temperature relationships of two boron-doped polysilicon resistors with doping concentration of 2×10^{20} cm^{-3}........................... 63

3.7 Measured V-I curves (symbols) of the sensors with different widths together with the fitted curves (solid lines) of Eq. (3.38)..................................... 64
3.8 The over-heat ratio of the sensors calculated from the measured I-V data are plotted against the square of the heating current. The solid lines are the fitted curves of Eq. (3.39).The fitting parameter $\bar{h}$ is found to be 0.262............ 65
3.9 Calculated temperature distribution (relative to room temperature) on the diaphragm of the 3.3 μm wide sensor at an over-heat ratio of 0.1. 66
3.10 Output voltage sensitivity of the sensor to ambient temperature in CC mode...... 67
3.11 Ambient temperature sensitivity of the sensor output voltage in CT mode. The sensor temperatures corresponding to the over-heat ratios of 0.05, 0.10 and 0.20 are 73°C, 123 °C and 223 °C respectively. 68
3.12 Output voltage changes as a function of heat transfer coefficient at different over-heat ratios for the 3.3 μm wide sensor. 71
3.13 Zoom-in of the calculated $\bar{V} - \Delta\bar{h}$ curves in the linear region. 72
3.14 Output voltage changes in CC mode at different over-heat ratios. The normalized output ($\Delta V/V_0$) increases dramatically with over-heat ratio. 72
3.15 Output voltage changes in CT mode at different over-heat ratios. The normalized output is almost insensitive to the over-heat ratio............................. 73
3.16 The drift of the sensitivity to heat transfer coefficient with ambient temperature in CT mode... 74
3.17 Wind-tunnel calibration results of the sensors with different width at the over-heat ratio of 0.1. 75
3.18 Circuit used in measuring the frequency response of the sensors in CC mode..... 76
3.19 Magnitude responses of $r_b(i\omega)$ for sensors with different widths......................... 78
3.20 Phase responses of $r_b(i\omega)$ for sensors with different widths. Note that the curves for 7 μm, 11 μm and 15 μm have been shifted down by 5, 10 and 15 degrees respectively to avoid overlapping with other curves.......................... 79
3.21 Magnitude responses of $G_h(i\omega)$. 80

3.22 Magnitude responses of $G_T(i\omega)$. 81

3.23 Magnitude responses of the gain of the CT circuit at $a_R = 0.1$. 85

3.24 Phase responses of the gain of the CT circuit. 86

3.25 Calculated frequency response of the sensitivity to heat transfer coefficient in CT mode. 87

3.26 Calculated frequency response of the temperature sensitivity in CT mode. 88

3.27 Structures and SEM pictures of other types of micromachined shear stress sensors. 90

3.28 Frequency responses of four types of sensors in CC mode. 91

3.29 Thermal resistance in atmosphere and in vacuum. The polysilicon resistors are all 120 μm long and 3 μm wide. The distance between the resistors and the substrates for types II, III and IV are 4 μm. 93

3.30 The power needed to heat up type IV sensors with different bridge height to 200°C. 94

3.31 Wind tunnel calibration results for all types of micromachined shear stress sensor structures in CT mode ($a_R = 0.1$). 95

4.1 Boundary layer development in channel flow. 100

4.2 Counter-rotating vortex pair. 102

4.3 The micromachined shear stress imager (2.85×1 cm^2) with over 100 sensors. 104

4.4 Photograph of the packaged shear stress imager. 105

4.5 Imaging chip package and wind tunnel setup. 105

4.6 Constant temperature biasing circuit, gain stage and temperature compensation stage. 106

4.7 Calibration curves of 10 sensors in a row. 107

4.8 Typical temperature sensitivities before and after temperature compensation of a shear stress sensor. 108

4.9 Turbulence statistics based on the shear stress fluctuations recorded by the micro shear stress sensors on the imaging chip. 110

4.10 Comparison between the instantaneous outputs from a shear stress on the flush-mounted imaging chip and a 1 mm long hot-wire anemometer 0.4 mm above the shear stress sensor at a centerline velocity of 10 m/s.. 111

4.11 Contour plot of the pseudo 2-D shear stress distribution. Red area indicates high shear stress and blue area indicates low stress. 112

4.12 Comparison of the contour plots obtained by using 4 rows of sensors (real 2-D imaging) and by using only one row of sensors (pseudo 2-D imaging) at a centerline velocity of 20 m/s. 113

4.13 Scales of the near-wall streaky structures at different Reynolds numbers. 115

4.14 Schematic drawing of the packaging for underwater shear stress imager. 117

4.15 Photograph of the packaged shear stress imager for underwater measurement. Note that the imager is not diced in the same way as that in Figure 4.3 and the surface surrounding the imager and the dummy Si chip is not flat because of the hand-painted epoxy. 117

4.16 Calibration results of a shear stress sensor in a water channel. 118

4.17 Instantaneous output voltage (with gain of 10) at a mean water flow speed of 25 cm/s. 118

5.1 Drag coefficient (defined as the normalized drag force to dynamic force) change with the phase of the actuator excited by sine wave with different frequencies 124

5.2 A 1×1 cm^2 prototype M^3 chip with integrated shear stress sensors, micro magnetic actuators and CMOS control circuits. 126

5.3 Simplified process flow the prototype M^3 chips. 127

5.4 Photograph of the low voltage shear stress sensor on a M^3 chip. The polysilicon wire is 15 μm wide and 150 μm long. The Newton rings are the result of the bending on the diaphragm by the vacuum underneath. 129

5.5 Deflection of diaphragms on top of vacuum cavities with (a) rigid and (b) soft supports. 129

5.6 The proposed design with 1 μm fully recessed LOCOS and greatly reduced surface roughness. The numbers are the surface levels relative to the silicon surface in unit of microns. 130

6.1 Si island shapes formed by different ways. 136

6.2 Simplified process flow of the new flexible skin technology. 137

6.3 Picture of a wafer-size flexible skin. 137

6.4 Fabrication process flow of the flexible shear stress sensor skin. 141

6.5 Photograph of a shear stress sensor. A square silicon nitride diaphragm ($200\times200\ \mu m^2$) with an embedded polysilicon wire is on top of a vacuum-sealed cavity. 142

6.6 Picture of a flexible shear stress sensor array (1 cm × 3 cm). 142

6.7 A flexible shear stress sensor skin sits on a conic object. The bending is caused by gravitation. 143

6.8 Schematic of the delta wing. 144

6.9 Packaging scheme for the flexible shear stress sensor skin on delta wing leading edge block. 145

6.10 Picture of a Si circuit board. 145

6.11 Two flexible skins wrapped around on a semi-cylindrical block, 2 cm long and 1.3 cm in diameter. 145

6.12 Calibration results of the sensors on flexible skins. 146

6.13 Flow separation at $\phi \approx 85^o$ on a cylinder is detected during the calibration. 147

6.14 Flow separation on the leading edges of a delta wing. 148

6.15 Picture of the skin-mounted delta wing model. 148

6.16 Averaged output from one row of sensors on a skin. 150

6.17 Output voltages (after gain of 10) from the sensors located before and after the flow separation point at velocity of 30 m/s. 150

6.18 RMS fluctuation used to identify separation point.. 151

6.19 Comparison of separation lines measured by a single sensor and a flexible....... 151

6.20 Layout design of the sensor-actuator skin for delta wing control. 152

6.21 Simplified process flow for the sensor-actuator skin... 153

6.22 Picture of the best sensor-actuator skin on a wafer.. 154

6.23 Cross-section of the proposed conformable M^3 system for delta wing control……………………………………………………………………………154

List of Tables

2.1 Comparison between conventional and micromachined hot wires. 43

3.1 Parameters calculated from measured *I-V* curves. 65

3.2 Calculated and fitted parameters for the study of dynamic responses. 77

3.3 Comparison of conventional and micromachined shear stress sensors. 89

6.1 Properties of DuPont Pyralin® PI-2808 polyimide. 138